Published in final edited form as:
Ann Neurol. 2014 December ; 76(6): 845–861. doi:10.1002/ana.24271.

Impairment of paravascular clearance pathways in the aging brain

Benjamin T. Kress[1,*], **Jeffrey J. Iliff**[1,2,3,*], **Maosheng Xia**[1,4], **Minghuan Wang**[1], **Helen Wei**[1], **Douglas Zeppenfeld**[2], **Lulu Xie**[1], **Hongyi Kang**[1], **Qiwu Xu**[1], **Jason Liew**[1], **Benjamin A. Plog**[1], **Fengfei Ding**[1,2], **Rashid Deane**[1], and **Maiken Nedergaard**[1]

[1]Center for Translational Neuromedicine, University of Rochester School of Medicine, Rochester NY

[2]Department of Anesthesiology and Perioperative Medicine, Oregon Health & Science University, Portland OR

[3]Knight Cardiovascular Research Institute, Oregon Health & Science University, Portland OR

[4]Department of Orthopedics, The First Hospital of China Medical University, Shenyang, 110001, People's Republic of China

Abstract

Objective—In the brain, protein waste removal is partly performed by paravascular pathways that facilitate convective exchange of water and soluble contents between cerebrospinal and interstitial fluids. Several lines of evidence suggest that bulk flow drainage via the glymphatic system is driven by cerebrovascular pulsation, and is dependent on astroglial water channels that line paravascular cerebrospinal fluid (CSF) pathways. The Objective of this study was to evaluate whether the efficiency of CSF-ISF exchange and interstitial solute clearance is impaired in the aging brain.

Methods—CSF-ISF exchange was evaluated by in vivo and ex vivo fluorescence microscopy while interstitial solute clearance was evaluated by radio-tracer clearance assays in young (2–3 month), middle age (10–12 month) and old (18–20 month) wild type mice. The relationship between age-related changes in the expression of the astrocytic water channel aquaporin-4 (AQP4) and changes in glymphatic pathway function were evaluated by immunofluorescence.

Results—Advancing age was associated with a dramatic decline in the efficiency of exchange between the subarachnoid CSF and the brain parenchyma. Relative to the young, clearance of intraparechamally injected amyloid β was impaired by 40% in the old mice. A 27% reduction in the vessel wall pulsatility of intracortical arterioles and widespread loss of perivascular AQP4 polarization along the penetrating arteries accompanied the decline in CSF-ISF exchange.

Corresponding Authors: Jeffrey J. Iliff, PhD, Department of Anaesthesiology and Peri-Operative Medicine, Oregon Health & Science University, 3181 SW Sam Jackson Park Rd., Mail Code HRC5N, Portland, OR 97239 USA, iliffj@ohsu.edu, Phone: (503) 494-4047, Maiken Nedergaard, MD, PhD, Center for Translational Neuromedicine, Box 645, 575 Elmwood Ave., Rochester, NY 14642 USA, Nedergaard@URMC.Rochester.edu, Phone: (585) 273-2868.
*These authors contributed equally to this work

Conflict of Interest: The authors declare that they have no competing conflict of interest

Interpretation—We propose that impaired glymphatic clearance contributes to cognitive decline among the elderly and may represent a novel therapeutic target for the treatment of neurodegenerative diseases associated with accumulation of mis-folded protein aggregates.

Introduction

Advancing age is the strongest risk factor for the development of many neurodegenerative diseases, including Alzheimer's disease (AD), Parkinson's disease (PD), Huntington's disease, fronto-temporal dementia and chronic traumatic encephalopathy (CTE). In the case of AD, incidence increases from approximately 12% in the 70s to more than 50% in the 80s (1).

A central histopathological hallmark of each of these diseases is the presence of mis-aggregated proteins, including senile plaques comprised of amyloid β (Aβ) in AD, neurofibrillary tangles comprised of hyperphosphorylated tau in AD and CTE, Pick bodies comprised of hyperphosphorylated tau in fronto-temporal dementia, α-Synuclein-containing Lewy bodies in PD, and intracellular inclusions of huntingtin in Huntington's disease (2).

Little is known regarding the pathogenic events that initiate protein aggregation in these different conditions. Age-related deposition of protein aggregates could result from accelerated production or slowed clearance of the protein, or alternatively from the introduction of a mis-folded template conformer that can seed aggregation. In the setting of AD, when Aβ production and clearance were measured and compared between AD patients and cognitively-normal individuals, rates of Aβ clearance were slowed in AD patients while rates of Aβ production were not altered (3). However, the cellular and molecular changes that impair Aβ clearance and render the aging brain vulnerable to Aβ plaque deposition remain unclear.

We have recently defined a brain-wide network of paravascular pathways that facilitates the efficient clearance of interstitial solutes, including Aβ, from the brain parenchyma. During sleep, subarachnoid cerebrospinal fluid (CSF) from the cisternal compartments rapidly recirculates through the brain along paravascular spaces surrounding penetrating cerebral arteries and exchanges with surrounding interstitial fluid (ISF) (4–6). ISF and interstitial solutes in turn are cleared along paravascular spaces surrounding large caliber cerebral veins. Paravascular bulk flow of CSF and ISF are supported by the astroglial water channel aquaporin-4 (AQP4) which is localized to perivascular astrocytic endfeet ensheathing the cerebral vasculature. Genetic deletion of *Aqp4* markedly impaired interstitial solute clearance, including reducing exogenous Aβ clearance by 65% (4).We have termed this pathway the 'glymphatic' system, owing to its dependence upon astroglial water transport and its assumption of the peripheral lymphatic function of interstitial solute clearance within the CNS.

In the present study, we evaluate whether the glymphatic pathway function, including the clearance of interstitial solutes such as Aβ, is impaired in the aging brain. Evaluating paravascular CSF recirculation through the brain parenchyma by in vivo 2-photon and ex

vivo fluorescence imaging and interstitial solute clearance by radio-tracer clearance assay, we report that glymphatic pathway function is dramatically impaired in the aging brain.

Methods

Animals

All experiments described in this study were approved by the University of Rochester Medical Center Committee on Animal Resources. Unless otherwise noted, 2–3 month, 8–10 month, and 18 month old male and female C57BL/6 mice acquired from Charles River and the National Institute of Aging were used in all experiments. In all experiments, animals were anesthetized with a combination of ketamine (0.12 mg/g intraperitoneally) and xylazine (0.01 mg/g intraperitoneally).

Fluorescent CSF Tracers

All CSF tracers were reconstituted in artificial CSF at a concentration of 0.5%. For co-infusion experiments, small molecular weight Texas Red conjugated dextran (TR-d3; 3 kDa) and large molecular weight Alexa 647 conjugated Ovalbumin (OA-647; 45 kDa) were mixed in a 1:1 ratio of 1% solutions. All fluorescent CSF tracers were acquired from Invitrogen.

Intracisternal Tracer Infusions

Mice were anesthetized and fixed in a stereotaxic frame while the posterior atlanto occipital membrane overlying the cisterna magna was surgically exposed. For all CSF tracer experiments, tracers were infused into the subarachnoid CSF via cisterna magna puncture, at a rate of 2 μL/min for a period of 5 minutes (10 μL total volume) through a 30 GA syringe pump (Harvard Apparatus). In prior studies, we have found that this rate and duration of tracer infusion does not cause reflux of subarachnoid CSF back into the ventricular CSF compartments, suggesting that the physiological direction of CSF bulk flow is maintained (4, 6, 7). We have observed that intracisternal CSF tracer infusion mildly increases intracranial pressure (ICP), however these effects persist only for the duration of tracer infusion and ICP normalizes rapidly after the cessation of infusion (7). Additionally, we have observed that at infusion rates that do not change ICP, paravascular CSF tracer flux follows the same patterns observed in the present study (5, 8). Because paravascular CSF recirculation occurs long after the normalization of ICP after the cessation of tracer infusion, the CSF tracer fluxes observed in the present study appear to represent the physiological movement of CSF along paravascular spaces after the tracer loading that occurs during the 5 min infusion period. To visualize penetration of fluorescent CSF tracers into the brain parenchyma ex vivo, anesthetized animals were trans-cardially perfusion fixed with 4% paraformaldehyde (PFA) at 30 minutes after the start of infusion, a time point previously identified to correspond to robust tracer penetration of similar molecular weight compounds in young male C57BL/6 mice (4). Brains were then dissected and post-fixed in 4% PFA for 24 hours before being sliced into 100 μm coronal sections using a vibrotome and mounted using PROLONG anti-fade gold with DAPI (Invitrogen). Tracer movement along perivascular spaces and permeation of the brain parenchyma was visualized in ex vivo studies by conventional fluorescence microscopy and confocal laser scanning microscopy.

Ex-vivo imaging of fluorescent CSF-tracers

Tracer recirculation along perivascular pathways and penetration into the brain parenchyma was visualized by conventional fluorescence microscopy of 100 μm vibratome coronal brain sections as described previously (4). In brief, 8 brain sections per animal were imaged and analyzed by a blinded investigator using an Olympus fluorescence microscopy under 4x objective power to generate whole-slice montages (using the Virtual Slice module of Microlucida software, MicroBrightfeild).

Tracer penetration was quantified using NIH Image J software as described previously (4). Briefly, fluorescence channels from each slice were split to separately measure fluorescence of co-infused small and large molecular weight Texas Red conjugated dextran (Dex-3; 3 kDa) and Alexa 647-conjugated ovalbumin (OA-45; 45 kDa). Brain regions of interest, including whole slice, dorsal cerebral cortex, lateral cerebral cortex, ventral cerebral cortex, caudate putamen (striatum), lateral septal nucleus, hippocampus, corpus callosum, thalamus, and hypothalamus, were defined using NIH Image J ROI manager. Fluorescent tracer coverage within each region was measured by uniformly thresholding each fluorescence channel and measuring the thresholded area as a % of the overall region area, as described previously (4). The fluorescence area coverage from the 8 brain slices from each animal were averaged to define CSF penetration within a single biological replicate. The effect of age on small and large molecular weight CSF tracer penetration was evaluated independently for each tracer using a 1-way ANOVA with Tukey's post-hoc test to determine differences between age groups. The relative changes in CSF tracer penetration were plotted by normalizing the small and large molecular weight tracer fluorescence intensity for the young, middle aged, and old groups to the fluorescence intensity of the young animals for each tracer. Size-dependent differences in the rate of decline in CSF tracer penetration were evaluated using a 2-way ANOVA with Sidak's post-hoc test to determine individual differences in the rate of decline with respect to the young animals

Intraparenchymal radio-tracer injections

Since there was no significant difference between the clearance of Aβ from brain using radio-iodinated Aβ and non-radio labeled Aβ (ELISA) (9), iodinated Aβ was used in these studies. Briefly, a stainless steel guide cannula was implanted stereotaxically into the right caudate nucleus of anesthetized mice with the cannula tip coordinates 0.7 mm anterior and 3 mm lateral to the bregma, and 1.3 mm below the surface of the brain. Animals were allowed to emerge from anesthesia and the experiments were conducted 10–18 hrs after guide cannula implantation, a time point that precedes the start of substantial inflammatory process, as assessed by histological analysis of tissue (negative staining for reactive astrocytes, GFAP, and reactive microglia, anti-phosphotyrosine), but allowed time for the BBB repair for large molecules, as reported (10, 11).

For the injection of the mixture of tracers, artificial CSF (0.5 μL) containing ^{125}I-labeled test-tracers Aβ (10 nM monomer) together with ^{14}C-inulin (0.05 μ Ci; reference molecule) was microinfused into brain ISF over 5 minutes. At the end of the experiments brain was removed and prepared for radioactivity analysis and TCA analyses. Our earlier studies

with ^{125}I-labeled Aβ have demonstrated that radiolabeled $A\beta_{1-40}$ remain mainly intact in brain ISF (> 95%) within 30–300 min of *in vivo* clearance studies.

For radioactivity analysis, ^{125}I radioactivity was determined in a gamma counter (Wallac Vizard Gamma Counter, Perkin Elmer). For ^{14}C- counting, the samples were solubilized in 0.5 ml tissue solubilizer (Perkin Elmer) overnight, followed by addition of 5 ml of scintillation cocktail (Packard Ultima Gold) and analyzed in a liquid scintillation counter (Beckman Coulter Counter). To differentiate between radioactivity originating from ^{14}C and ^{125}I, the counting window for measuring radioactivity was set to remove ^{125}I spillover, while a sample containing ^{125}I-$A\beta_{1-40}$ equivalent to that which was present in the injectate was measured in parallel with each experiment to monitor spillover of ^{125}I radioactivity into the ^{14}C counting window.

All calculations of clearance parameters were performed as reported previously (4, 6, 10). Briefly, the percentage of radioactivity remaining in the brain after microinjection was determined as % recovery in brain = $100\times(N_b/N_i)$ (eq. 1), where, N_b is the radioactivity remaining in the brain at the end of the experiment and N_i is the radioactivity injected into the brain ISF, i.e., the d.p.m. for ^{14}C-inulin and the c.p.m. for the TCA-precipitable ^{125}I-radioactivity. Inulin was used as a metabolically inert polar molecule which is neither transported across the BBB nor retained by the brain. The percentage clearance of ^{125}I-Aβ or ^{14}C-inulin was calculated from the total, as 100- brain recovery). Differences between ages in of ^{125}I-Aβ or ^{14}C-inulin clearance were evaluated by 1-way ANOVA with Tukey's post hoc test for multiple comparisons.

In vivo 2-photon fluorescence imaging

Tracer penetration into the intact living brain was visualized through a closed cranial window using a custom built 2-photon laser scanning (Olympus) microscope, as described previously (4). Animals were anethestized, intubated, and ventilated with a small animal ventilator (CWE) while blood gasses and pH were monitored and body temperature maintained at physiological parameters (~100 breaths/min, tidal volume of 0.3–0.4 ml, pO2 = 80–150mmHg, pH 7.25–7.5, body temperature of 37°C). Unilateral craniotomy (3mm in diameter) was performed over the cerebral cortex, 1mm lateral and 0.5mm posterior to bregma. Care was taken to ensure the dura was not ruptured. Immediately following the craniotomy the dura was covered with aCSF and the craniotomy sealed with glass coverslip. The femoral artery was then cannulated for mean arterial blood pressure monitoring and the measurement of arterial blood gas values. Only mice with blood gases within the physiological range were included in the present study. To visualize the vasculature, 0.1ml BBB impermeable Texas Red-dextran 70 (MW 70kD; 1% in saline, Invitrogen) was injected intra-arterially immediately before imaging.

A Mai Tai laser (SpectraPhysics) attached to a confocal scanning system (Fluoview 300, Olympus) and an upright microscope (IX51W, Olympus) was used for in vivo imaging as described previously (4). A 20X (0.9NA) water immersion lens was used to image the cortex, from the surface to a depth of ~250μm. Excitation wavelength was 870nm for FITC and Texas Red. For FITC and Texas Red, emission was collected at 575–645nm. The cerebral vasculature was first imaged with 512×512 pixel frames from the surface to a depth

of 240μm with 5μm z-steps. After intracisternal injection of CSF tracer, tracer movement into the cortex was conducted with dual-channel (FITC and Texas Red) 512×512 pixel image acquisition. The cortex was repeatedly scanned from the surface to 240μm below the surface with 20μm z-steps at 1 minute intervals for the duration of the experiment. Image analysis was conducted in with ImageJ software (NIH) with the UCSD plugin set. After imaging, penetrating arterioles were distinguished from penetrating venules on the basis of morphology: surface arteries passing superficially to surface veins and exhibiting less branching at superficial cortical depths. Imaging planes 100–120μm below the cortical surface were selected for the analysis of intracisternal tracer penetration. To define tracer movement into paravascular brain tissue, donut-shaped ROIs were defined that had an external diameter of 150 pixels and an internal diameter of 50 pixels (thus excluding the vessel). These were centered upon the penetrating arterioles. Mean pixel intensity within these ROIs was measured at each time point. Within each animal at each time point para-arteriolar ROIs were separately averaged to generate values for a single biological replicate. When tracer movement along penetrating arterioles was compared, a 2-way repeated measures ANOVA was used followed by Sidak's test for multiple comparisons.

Measurement of Cerebrovascular Pulsatility

Cerebral vascular pulsatility was evaluated by in vivo 2-photon microscopy as described previously (7). To measure vessel diameters, 3000 ms *X–T* line scans were acquired orthogonal to the vessel axis in surface arteries, surface veins, penetrating arteries, and penetrating veins (Figure 3B). Penetrating vessel line scans were acquired 50–150 μm below the cortical surface. Vessel diameter was extracted from *X–T* plots (Figure 3C) by and plotted versus time using custom Matlab and ImageJ software. Steady-state vessel diameters were calculated as the mean value over the 3000 ms epoch. Vessel wall pulsatility (derived units μm*s) was calculated as the absolute value of area under the diameter–time plot, integrated about the running average over the 3000 ms epoch. Differences in vessel pulsatility between different vessel types was evaluated by one-way ANOVA, with Tukey's *post hoc* test to evaluate differences between vessel segments. The effect of treatment on vascular pulsatility and diameter was evaluated by two-way ANOVA, with Tukey's *post hoc* test for multiple comparisons.

Tetramethylammonium (TMA) Microiontophoresis Measurement of Extracellular Volume

All experimental procedures were adapted from the previous studies (6, 12). The single barrel iontophoresis microelectrode (tip diameter of 2–3 μm) contained 150 mM tetramethylammonium (TMA)-chloride and 10 μM Alexa 488. A series of currents of 20 nA, 40 nA and 80 nA were be applied by a dual channel microelectrode pre-amplifier. For measurements of TMA, microelectrodes with an outer diameter of 2–3 μm were fabricated from double-barreled theta-glass using a tetraphenylborate-based ion exchanger. The TMA barrel was backfilled with 150 mM TMA chloride, while the reference barrel contained 150 mM NaCl and 10 μM Alexa 568. All recordings were obtained by inserting the two electrodes to a depth of 150 μm below the cortical surface. Recording electrodes were inserted 2.5 mm lateral and 2 mm posterior to bregma. The electrode tips were imaged after insertion using 2-photon excitation to determine the exact distance between the electrodes (typically ~150 μm). The TMA signal was calculated by subtracting the voltage measured

by the reference barrel from the voltage measured by the ion-detecting barrel using a dual-channel microelectrode pre-amplifier. The Nikolsky equation was used for calibration of the TMA electrodes based on measurements obtained in electrodes containing 0.5, 1, 2, 4, and 8 mM TMA-chloride in 150 mM NaCl. The TMA measurements were acquired relative to similar recordings obtained in 0.3% agarose prepared from a solution containing 0.5 mM TMA and 150 mM NaCl. A custom-made MatLab software, 'Walter', developed by C. Nicholson was used to calculate α and λ values (6, 12). Differences in extracellular volume fraction and tortuosity were evaluated by 2-way ANOVA with Sidak's multiple comparisons test.

Evaluating regional CSF tracer penetration, AQP4 and GFAP immunofluorescence

Free floating immunofluorescence staining of 100 μm fixed coronal brain sections was performed to evaluate protein expression patterns of aquaporin-4 (AQP4) and glial-fibrillary acidic protein (GFAP) Slices were blocked with 3% normal donkey serum for 1 hour at room temperature, incubated overnight with primary antibody (rabbit anti-AQP4, 1:500; mouse anti-GFAP, 1:500, both from Millipore) and again incubated for 2 hours at room temperature with secondary antibody (Cy3-conjugated donkey anti-mouse antibody; Cy2-conjugated donkey anti-rabbit antibody; both 1:500; Jackson Immunoresearch).

GFAP and AQP4 expression were evaluated regionally in slices taken from animals injected intracisternally with ovalbumin-conjugated ALEXA 647, then perfusion-fixed 30min post-injection. In this way, GFAP- and AQP4-immunofluorescence could be evaluated in the same animals and brain regions in which CSF tracer penetration was measured. 3-channel whole-slice montages were generated at 4X magnification as above from one anterior and one posterior brain slice from each animal. Fluorescence channels were split and CSF tracer penetration was evaluated as detailed above and as described previously in each brain region. Regional GFAP expression, AQP4 expression and AQP4 polarization were similarly evaluated as described previously (13, 14). To measure regional GFAP expression, regions were uniformly thresholded and the area coverage of GFAP-immunoreactivity (as a % of the whole region area) was measured. To evaluate global AQP4 expression levels, mean AQP4 immunofluorescence intensity was measured within each region. To measure perivascular AQP4 polarization, the median immunofluorescence intensity of perivascular regions was measured. Then a threshold analysis measured the % of the region exhibiting AQP4 immunofluorescence greater than or equal to perivascular AQP4 immofluorescence (AQP4 % Area). 'Polarization' was expressed as the % of the region that exhibited *lower* AQP4-immunoreactivity than the perivascular endfeet ('Polarization' = 100 – AQP4 % Area). Hence AQP4 'Polarization' is a relative measurement of AQP4 localization: increasing polarization indicating higher perivascular AQP4-immunoreactivity relative to lower parenchymal AQP4-immunoreactivity, whereas reduced polarization indicating lower perivascular AQP4-immunoreactivity relative to higher parenchymal AQP4-immunoreactivity. Differences in regional GFAP expression, AQP4 expression, AQP4 polarization and CSF tracer penetration were evaluated by 2-way repeated measures ANOVA with Sidak's test for multiple comparisons.

Evaluating AQP4 and GFAP localization at perivascular endfeet and glial limitans

GFAP and AQP4 expression, in addition to CSF tracer penetration were further evaluated by laser scanning confocal microscopy at 20X objective power to generate 3-channel fluorescence images of the pial surface and cerebral vasculature in the lateral cerebral cortex. These were acquired in 40–60 μm Z-stacks (2 μm Z-steps). To evaluate immunolabeling surrounding cerebral blood vessels, 25×500 pixel rectangular ROS were generated that extended from the vessel wall into the surrounding brain tissue orthogonal to the vessel axis. Pixel intensities were averaged across the narrow axis of this ROI to generate a single linear plot of fluorescence extending from the vessel wall into the surrounding brain tissue for each vessel (Figure 5A-B). Additionally, immunofluorescence within perivascular endfeet (the region immediately abutting the blood vessel) was evaluated for each vessel. In this way, GFAP- and AQP4-immunoreactivty in tissue surrounding penetrating cerebral arterioles and intraparenchymal cerebral capillaries were evaluated. Differences in AQP4 and GFAP immunofluorescence in ROIs extending outward from brain blood vessels were evaluated by 2-way repeated measures ANOVA. Differences between perivascular AQP4- and GFAP-immunofluorescence were compared by an un-paired t-test.

To investigate immunolabeling at the brain pial surface, linear ROIs were generated in the same manner extending inward from the brain surface (Figure 9C) and GFAP- and AQP4-immunoreactivty relative to the cortical surface was plotted and averaged between slices and animals. Similarly, CSF tracer penetration across the pial surface was evaluated by analyzing ROI values from the fluorescence corresponding to the injected ovalbumin-conjugated ALEXA-647. Differences in AQP4 and GFAP immunofluorescence and CSF tracer fluorescence intensity in ROIs extending inward from the cortical surface were evaluated by 2-way repeated measures ANOVA.

Results

Glymphatic pathway function is impaired in the aging brain

We first evaluated whether glymphatic pathway function is impaired in the aging brain. For these experiments, young (2–3 month), middle-aged (10–12 month) and old (18 month) male C57Bl/6 mice were utilized. To evaluate paravascular CSF penetration into the brain parenchyma, 2 fluorescent CSF tracers (small molecular weight Texas Red-conjugated dextran, MW 3 kD, Dex-3; large molecular weight ovalbumin-conjugated ALEXA 647, MW 45 kD, OA-45) were slowly co-infused into the subarachnoid CSF of the cisterna magna (Figure 1A). Thirty minutes after the start of CSF tracer infusion, animals were perfusion-fixed, the brains sliced, and tracer penetration was evaluated by whole-slice 2-channel fluorescence imaging. Compared to the young mice, CSF tracer penetration into the both the middle-aged and old brain was significantly reduced, with the greatest effect in the old brains (Figure 1B, *$P<0.05$, ***$P<0.001$; 1-way ANOVA with Tukey's post hoc test for multiple comparisons; $n = 5–8$ animals per group). Representative images shown in Figure 1C demonstrate that in the middle-aged and to a greater extent in the old brain, CSF tracer penetration both along paravascular pathways and across the pial surface were dramatically reduced.

To evaluate whether interstitial solute clearance is impaired in the aging brain, we measured the clearance of intraparenchymally-injected radio-tracers. Radiolabeled ^{125}I-Amyloid $\beta_{1–40}$ and ^{14}C-Inulin (MW ~5kD) were co-injected into the caudate nucleus and after 60 min the clearance of both radio-tracers was measured by gamma counting and liquid scintillation counting, respectively (Figure 1D). The clearance of ^{14}C-Inulin, which is not cleared across the blood brain barrier (BBB) and is thus cleared by bulk flow alone (15) was significantly impaired in both the middle-aged and old mouse brain (Figure 1E, *P<0.05, **P<0.01; 1-way ANOVA with Tukey's post hoc test for multiple comparisons; n = 6–11 per group). The clearance of ^{125}I-Amyloid $\beta_{1–40}$, which is dependent both upon receptor-mediated trans-BBB clearance (15) as well as AQP4-dependent bulk flow(4, 14), was similarly impaired in both the middle-aged and old brain (Figure 1E, ***P<0.001, 1-way ANOVA with Tukey's post hoc test for multiple comparisons; n = 6–11 per group).

The dynamics of paravascular CSF-ISF exchange were evaluated in vivo by 2-photon microscopy following intracisternal injection of fluorescent CSF tracer (FITC-conjugated dextran, MW 40kD; Dex-40; Figure 2A). The cerebral vasculature was visualized through a closed cranial window after intra-arterial injection of Texas Red-conjugated dextran (MW 70kD, Dex-70) and penetrating arteries and veins were identified morphologically. When fluorescent CSF tracer penetration was evaluated 100μm below the cortical surface in the young brain, rapid accumulation of CSF tracer began within 5 min of injection and peaked ~50 min after injection (Figure 2B). In the middle-aged brain, CSF tracer penetration was markedly delayed compared to the young brain (Figure 2B; *P<0.05, 2-way repeated measures ANOVA with Sidak's multiple comparisons test; n = 4 animals per group). The slowing of paravascular CSF recirculation first along the cerebral surface vasculature, then along cerebral penetrating arterioles and into the surrounding interstitium is clearly evident in representative time-lapse images taken from young (Figure 2C) and middle-aged (Figure 2D) animals at the level of the cortical surface and 100 μm below the cortical surface.

Cerebral arterial pulsatility is impaired in the aging brain

The recirculation of CSF into the brain parenchyma along paravascular pathways is driven in part by arterial pulsation (5–7, 13, 16, 17). We next evaluated pulsation of the cerebrovascular wall by in vivo 2-photon microscopy. The cerebral vasculature was visualized by intra-arterial injection of Texas Red-conjugated dextran (70kD) visualized through a thin-skull cranial window preparation (Figure 3A). Small changes in vessel diameter were measured by high-frequency linescanning of penetrating arteries, and ascending veins between 0–150μm below the cortical surface. As we have recently described (7), a value for 'vascular pulsatility' was extracted from X-t (diameter-time) plots (Figure 3B-C), derived from the dilation of the vessel diameter with each cardiac cycle, and integrated across a 3000 ms epoch. In agreement with our prior findings (7), we observed that within the young brain the vessel wall pulsatility of penetrating arteries was significantly greater than the pulsatility of ascending veins (Figure 3D; *P<0.05, Penetrating arteries vs. Ascending veins; 2-way ANOVA with Tukey's post hoc test for multiple comparisons; n = 8–20 vessels from 4 animals per group). When vascular pulsatility was evaluated in the old (18 months) cortex, we observed that the pulsatility in deep penetrating arteries was significantly reduced compared to that in the young cortex (Figure 3D; *P<0.05,

Young vs. Old; 2-way ANOVA with Tukey's post hoc test for multiple comparisons; n = 8–20 vessels from 4 animals per group). In contrast to penetrating arteries, no age-related changes in vascular pulsatility were observed in ascending veins, (Figure 3E). These data suggest that age-related reductions in penetrating arterial pulsatility may underlie the impairment of paravascular CSF recirculation in the aging brain.

Extracellular volume regulation of the interstitial space is unchanged in the aging brain

Paravascular CSF-ISF exchange is a feature of the sleeping brain. In the awake state, the rate of paravascular CSF recirculation is reduced by ~95% compared to that observed in the brain undergoing natural sleep or anesthesia, while the clearance of interstitial solutes such as amyloid β from the awake brain is more than 2-fold slower than in the sleeping or anesthetized state (6). This appears to be attributable to a 60% expansion in the extracellular volume during sleep, which presumably lowers the total tissue resistance to convective CSF fluxes, facilitating the movement of fluid and solutes through the brain interstitium (6). Thus, in the present study, we sought to evaluate whether a changes in the extracellular space may account for the impaired CSF-ISF exchange in the aging brain. To test this hypothesis, we used in vivo cortical TMA iontophoresis (6, 18) to measure whether the dimensions (extracellular volume fraction, α) or characteristics (tortuosity, λ) of the extracellular space are altered in the aging brain (Figure 4A). In each animal, α and λ values were measured first in the awake state. Animals were then anesthetized and α and λ values were measured a second time to generate paired awake/anesthetized recordings. When extracellular volume fraction were measured, we found that in both the awake and the anesthetized state no significant differences were apparent between the young and the old brains (Figure 4B; P = 0.4957, Young vs. Old; 2-way ANOVA with Sidak's multiple comparisons test; n = 9–20 per group). However, the significant expansion of the extracellular space between the waking and the anesthetized state was observed both within the young and the old brain (Figure 4B; ***P<0.001). When extracellular tortuosity was measured, there were no significant effects of age upon lambda values in either the waking and anesthetized state (Figure 4C; P = 0.3375, Young vs. Old; 2-way ANOVA with Sidak's multiple comparisons test; n = 9–20 per group).Thus, the expansion of the extracellular space in the anesthetized state is maintained in the aging brain which suggests that extracellular volume regulation likely does not explain the dramatic reduction in CSF-ISF exchange observed in old vs young mice.

Perivascular AQP4 polarization is impaired in the aged brain

AQP4, an astroglial water channel, is localized in a highly polarized manner to endfoot processes surrounding the cerebral vasculature in addition to the *glial limitans externa* which abut the pia mater and bound the subarachnoid CSF compartment (19, 20). The perivascular astrocytic endfeet completely ensheath the cerebral vasculature, leaving on 20nm gaps between overlapping processes (21–23). Along these processes, as much as 50 percent of the vessel-facing membrane is populated by crystalline plaques (termed 'orthogonal arrays of particles') of AQP4 water channels (24). We have previously demonstrated that perivascular AQP4 facilitates paravascular CSF-ISF exchange (14), and have proposed that the loss of perivascular AQP4 polarization in the injured brain may contribute to the impairment of glymphatic pathway function (13, 14, 16). In the present

experiments, we evaluated whether perivascular AQP4 polarization is lost in the aging brain, and whether changes in AQP4 localization differed between perivascular domains surrounding large penetrating arterioles and surrounding microvessels..

Figure 5 shows the differences in perivascular GFAP and AQP4 expression and localization in the young (Figure 5A) and old (Figure 5B) cortex. AQP4 and GFAP immunofluorescence intensity was measured along linear ROIs extending outward from the lumen of penetrating cerebral arterioles or cerebral capillaries, averaged between vessels in the young and old cortex, then plotted as a function of distance from the vessel wall. In the young cortex, AQP4 immunofluorescence surrounding penetrating arterioles and capillaries was highly polarized, with low levels of expression up to the margin of the perivascular endfeet where expression was high (Figure 5C-D). In the old cortex, AQP4 immunofluorescence increased markedly in the tissue immediately surrounding penetrating arterioles (Figure 5C; ***$P<0.001$ young vs. old, 2-way repeated measures ANOVA; n = 11–12 vessels from 4 animals per group) while AQP4 expression surrounding capillaries was generally elevated, was not as pronounced as in the tissue surrounding penetrating arterioles (Figure 5D). AQP4 expression in the perivascular endfeet immediately surrounding penetrating arterioles was significantly reduced in the old compared to the young brain (Figure 5E; *$P<0.05$; un-paired t-test, n = 11–18 vessels from 4 animals per group), while no significant difference in AQP4 expression were observed in perivascular endfeet surrounding cerebral capillaries.

Within the same ROIs, GFAP expression was also significantly higher surrounding penetrating arterioles (Figure 5F) and cortical capillaries (Figure 5G; *$P<0.05$, 2-way repeated measures ANOVA, n = 11–18 vessels from 4 animals per group). Quantification of GFAP expression in perivascular endfeet revealed significantly elevated expression in perivascular endfeet surrounding both penetrating arterioles and capillaries (Figure 5H; ***$P<0.001$, un-paired t-test; n = 11–18 vessels from 4 animals per group). These results show that the development of diffuse reactive astrogliosis is a general feature of the aging brain. In contrast, the changes in AQP4 expression in the aging brain is more specifically distributed, with marked upregulation of AQP4 and loss of perivascular AQP4 polarization in brain tissue immediately surrounding penetrating cortical arterioles.

We next evaluated whether different brain regions exhibited distinct patterns of AQP4 expression or localization, or reactive astrogliosis with advancing age. Slices from the anterior (Figure 6A-C) and posterior (Figure 6D-F) brains of young (2–3 months) and old (18 months) mice fixed 30 min after intracisternal CSF tracer (OA-45) injection were stained for AQP4 and GFAP. Slices were imaged by 3-channel whole-slice fluorescence microscopy and divided into region-specific ROIs for analysis of AQP4 expression (mean AQP4 immunofluorescence intensity, Figure 6A, D), AQP4 polarization (proportional localization of AQP4 to perivascular vs. parenchymal domains (13, 14), Figure 6B, E) and GFAP expression (% coverage of GFAP immunoreactivity, Figure 6C, F). To show differences in these values, we generated heat maps that show the change in mean AQP4 expression, AQP4 polarization or GFAP expression within each brain region between young and old brains. Global AQP4 expression within each brain region did not significantly change when compared between young and old anterior or posterior brain slices (Figure 6A, D, respectively). In contrast, perivascular AQP4 polarization in the old brains was

consistently and significantly reduced compared to the young brains throughout both anterior (Figure 6A) and posterior (Figure 6E) brain regions (*P<0.05, ***P<0.001, Young vs. Old; 2-way repeated-measures ANOVA with Sidak's multiple comparisons test; n = 4 animals per group). These effects were most consistent within the lateral and ventral cortex, while marked loss of AQP4 polarization was also observed in the aged versus the young hippocampus. Development of reactive astrogliosis, identified by increasing GFAP expression, was similarly apparent throughout the aging brain (Figure 6C, F; *P<0.05, **P<0.01, Young vs. Old; 2-way repeated-measures ANOVA with Sidak's multiple comparisons test; n = 4 animals per group). As with AQP4 mis-localization, the most pronounced elevation of GFAP expression was in the lateral and ventral cortex and in the hippocampus of the aged compared to the young brain.

Loss of perivascular AQP4 polarization is associated with glymphatic pathway impairment

Paravascular CSF recirculation was evaluated 30 min after intracisternal CSF tracer injection. In the same sections in which GFAP expression, AQP4 expression and perivascular AQP4 polarization were measured, As shown in Figure 7A-B, representative sagittal and coronal slices fixed 30 min after injection of small molecular weight (Dex-3) and large molecular weight (OA-45) CSF tracer exhibited marked reduction of paravascular CSF penetration in the old compared to the young brain. Quantification of OA-45 penetration between anterior and posterior brain regions (Figure 7C,D) showed that age-related impairment of glymphatic CSF recirculation was restricted primarily to the cortex, with the greatest decline evident within the lateral and ventral cortex, particularly in posterior brain regions (Figure 7C,D, *P<0.05, **P<0.01, ***P<0.0001, Young vs. Old; 2-way repeated-measures ANOVA with Sidak's multiple comparisons test; n = 4 animals per group).

We have proposed that loss of perivascular AQP4 polarization underpins age-related impairment of glymphatic pathway function. In principal, global changes in AQP4 expression or the development of reactive astrogliosis might also drive the impairment of paravascular CSF recirculation. To determine whether changes in AQP4 expression, AQP4 polarization or GFAP expression are most closely associated with impaired CSF tracer penetration, we performed linear regression analysis on paired data from cortical ROIs that comprised Figure 6 and Figure 7C,D. Linear regression (Figure 8) revealed no significant association between cortical GFAP expression and CSF tracer penetration in either the young ($P = 0.3992$; $r^2 = 0.0377$) or the old ($P = 0.6061$; $r^2 = 0.0143$) brain. Similarly, global cortical AQP4 expression was not significantly related to CSF tracer penetration in either the young ($P = 0.0501$; $r^2 = 0.1634$) or the old ($P = 0.2301$; $r^2 = 0.0749$) brain. Loss of cortical AQP4 polarization, however, was significantly associated with impairment of CSF tracer penetration both in the young and in the young ($P = 0.0225$; $r^2 = 0.2149$) or the old ($P = 0.0215$; $r^2 = 0.2485$) brain. It is important to note that these data provide correlative evidence that support the hypothesis that loss of perivascular AQP4 polarization contributes to age-related impairment of glymphatic pathway function. They do not, however, directly test this hypothesis. Additionally, when data were pooled between young and old animals, the negative association between AQP4 polarization and CSF tracer penetration disappeared. This suggests that while changes in AQP4 polarization are likely important drivers of

glymphatic pathway function, other age-related factors also appear to contribute to the impairment of glymphatic pathway function with age. These might include age-related declines in cerebral arterial pulsatility described in the present study, or age-related slowing of CSF turnover (25).

In addition to its polarized expression in perivascular astrocytic endfeet, AQP4 is also intensely expressed in the *glial limitans externa* at the cortical surface. This interface between the subarachnoid CSF space and the interstitium is a major route for the recirculation of CSF into and through the brain interstitium (4, 6). Within the same slices analyzed above, we evaluated the relationship between age-related changes in AQP4 expression, GFAP expression, and CSFS tracer penetration near the *glial limitans*. Figure 9A-B depicts representative images from the young and old dorsal cortex. As shown in Figure 9C, AQP4 expression near the pial surface is markedly increased in the aged brain, which coincides with a marked impairment of CSF tracer penetration (Figure 9A-B, bottom panel). AQP4- and GFAP-immunofluorescence and CSF tracer intensity were quantified along linear regions of interest (ROIs) extending inward from the cortical surface and averaged between 6–8 ROIs taken from 4 animals (Figure 9C-D). In the aging brain, AQP4 expression was significantly increased near the pial surface (**$P < 0.01$, Young vs. Old; 2-way repeated measures ANOVA), while CSF tracer penetration across the pial surface was significantly reduced (**$P < 0.01$, Young vs. Old; 2-way repeated measures ANOVA). GFAP expression near the pial surface tended to be higher in the old compared to the young brain, although in contrast to AQP4, this difference was not significant when measured between all samples in all animals.

In total, these data show that age-related loss of perivascular AQP4 polarization and AQP4 polarization at the cortical surface is associated with the impairment of paravascular CSF tracer penetration, and that this impairment is most pronounced in the cerebral cortex. These findings support the notion that mis-localization of AQP4 contributes to the glymphatic pathway dysfunction in the aging brain.

Discussion

We have recently demonstrated that the rapid exchange of CSF and ISF along paravascular pathways facilitates the clearance of interstitial solutes, including Aβ, from the brain parenchyma (4–7). Primarily active in the sleeping brain, this network of paravascular channels has been termed the ‘glymphatic’ pathway due to its dependence upon astroglial water transport and its assumption in the brain of the lymphatic function of interstitial solute elimination. In the present study, we tested the hypothesis that impairment of glymphatic pathway function in the aging brain slows the clearance of interstitial Aβ, rendering the aging brain vulnerable to neurodegenerative disease.

In vivo two photon and ex vivo whole-slice fluorescence microscopy were used to directly visualize the efficiency of convective exchange between paravascular CSF and brain ISF in aging wild type mice. Both paravascular CSF tracer recirculation and interstitial radio-tracer clearance were impaired in the aging brain, with Aβ clearance from the aged brain reduced by 40% compared to the young brain. Impairment of glymphatic pathway function was

accompanied by a 27% reduction in cerebral arterial wall pulsatility, which is an important contributor to paravascular flux along the glymphatic pathway (7, 17, 26). In addition, we show that impairment of paravascular CSF-ISF exchange is similarly associated with loss of perivascular localization of the astroglial water channel AQP4, a key determinant of glymphatic pathway activity (4).

The pulsation of cerebral arteries is a driving force for paravascular CSF-ISF exchange (7, 17, 26–28). Interestingly, age-related changes in cerebrovascular function and structure have been implicated in the development of Alzheimer's disease and vascular dementia (29). In human cerebral arteries, vascular wall compliance is reduced as a function of age (30) while a recent clinical study demonstrated that loss of peripheral vascular compliance is associated with increased Aβ deposition in patients with mild cognitive impairment (31). Loss of arterial wall compliance is the most facile explanation for the observed age-related decline in vascular pulsatility. A second possibility, however, is that factors extrinsic to the cerebral vessels themselves account for this reduction in pulsatility. Pulsatility of the cerebral arterial wall occurs within the confines of the paravascular and perivascular spaces, which are closely enclosed within the pial sheath (32) and the perivascular astroglial endfoot sheath (22), respectively. Age-related changes in the compliance of these structures, such as might occur with the onset of reactive astrogliosis, may influence cerebrovascular pulsatility. Similarly, the freedom of fluid volume to move rapidly into and out of the perivascular spaces with each cardiac cycle may influence the deflection of the vessel wall through these spaces. Thus, age-related changes in perivascular AQP4 polarization may exert an effect upon arterial wall pulsatility along penetrating cerebral arterioles. These intriguing possibilities clearly warrant further investigation. The present observation that a decline in cerebral arterial wall pulsatility accompanies the impairment of paravascular CSF-ISF in the aging brain suggests that the impairment of glymphatic pathway function may be one mechanism linking changes in cerebrovascular structure and function with the onset of neurodegeneration and dementia.

In a prior study, we observed that dynamic changes in the brain extracellular volume fraction are key regulators of glymphatic pathway function during the sleep-wake cycle, greater extracellular volume fraction during sleep facilitating the exchange of paravascular CSF with ISF (6). The decline in glymphatic pathway activity in old mice, however, did not result from changes in the brain extracellular space. Real-time TMA iontophoresis demonstrated that the sleep-wake differences in extracellular volume remained intact in the aging brain.

Paravascular CSF recirculation and ISF solute clearance is dependent upon the astroglial AQP4 water channel (4), which is localized primarily to perivascular astrocytic endfeet and astrocytic processes of the *glial limitans* and reduce the resistance to water flux across astrocytic endfeet (33). Reactive astrogliosis, a feature of the aging brain (34), is associated in several injury models with the loss of perivascular AQP4 polarization, as AQP4 distributes along non-perivascular fine astrocytic processes (13, 14). On the basis of these observations we tested here whether the loss of AQP4 polarity contributes to the dramatic decline in CSF recirculation in old mice.

We found that widespread astrogliosis and the loss of perivascular AQP4 polarization was evident throughout the aged brain, particularly within the cortex. Neuroinflammation and reactive astrogliosis are prominent features of the aging brain and hallmarks of neurodegerative disease (34–36), yet the functional consequence of neuroinflammatory changes in the aging brain are not well understood. Our analysis showed that reactive astrogliosis was generally associated with a loss of paravascular AQP4 expression, however this effect was most pronounced in the astrocytes surrounding the paravascular spaces of small penetrating arterioles. Correlation analysis between GFAP expression, AQP4 expression and perivascular AQP4 polarization with paravascular CSF recirculation in young and old brains showed that only the loss of perivascular AQP4 polarization was significantly associated with the impairment of CSF-ISF exchange in the cerebral cortex. This analysis supports the hypothesis that loss of perivascular AQP4 polarization along penetrating arteries impairs bulk flow along paravascular spaces in the aging brain. This loss of perivascular AQP4 polarization likely contributes to the observed impairment of interstitial solutes, including Aβ, as a substantial proportion of interstitial Aβ clearance is dependent upon perivascular AQP4 (4). This finding may also help to explain the observation that CSF turnover decrease and CSF protein concentrations increase in the aging brain (37). A substantial fraction of subarachnoid CSF recirculates through the brain parenchyma along paravascular pathways, and AQP4-dependent fluid movement along these pathways is an important contributor to solute clearance from the ISF. Thus, slowing of CSF and protein recirculation along these paravascular pathways may slow apparent CSF clearance and increase CSF protein levels in the aging brain. These findings suggest that the decline in glymphatic pathway function in the aging brain may contribute to the age-related Aβ deposition observed in sporadic forms of AD. Here it is intriguing to note that peripheral inflammation likewise slows interstitial bulk flow and the clearance Aβ from the brain (38). Based upon these findings, it is possible that peripheral inflammation may impair glymphatic pathway function and may contribute to the present age-related decline in paravascular CSF-ISF exchange.

Prior histopathological studies in both clinical AD cases and in transgenic models of AD have demonstrated that amyloid plaque deposition causes a loss of perivascular AQP4 polarization (35, 36). These and the present findings suggests that age-related changes in perivascular AQP4 polarization, impaired glymphatic clearance of Aβ, and amyloid plaque deposition may constitute a vicious feed-forward cycle driving amyloid aggregation and the development of neurodegeneration in the aging brain.

In addition to paravascular pathways of Aβ clearance, the clearance of Aβ by blood brain barrier transporters such as low density lipoprotein receptor-related protein 1 (LRP1), are major contributors to Aβ efflux from the brain (15). We surmise that these are likely overlapping processes. Within the micron-scale dimensions of the neurovascular unit, diffusion is sufficiently efficient to deliver solutes, such as Aβ to the local blood brain barrier. However, over greater distances, such as the millimeter-centimeter scales that separate areas of the brain interstitium from distant CSF compartments, bulk flow must facilitate the clearance particularly of peptide-and protein-sized interstitial solutes (39, 40). One possibility is that a substantial proportion of interstitial Aβ is cleared locally across the BBB, while Aβ in excess of BBB efflux transporter capacity is cleared by bulk flow along

paravascular pathways. A related possibility is that paravascular bulk flow within the brain parenchyma distributes interstitial Aβ to the BBB across a wider anatomical area, facilitating trans-BBB efflux. In this way efflux of Aβ across the BBB and glymphatic clearance of Aβ may in fact represent complimentary and partially overlapping mechanisms for the clearance of interstitial solutes such as Aβ from the brain.

The aggregation of mis-folded proteins is a factor common to several neurodegenerative disorders, including AD, amyotrophic lateral sclerosis (ALS), Parkinson's disease, Huntington's disease and chronic traumatic encephalopathy (CTE) (41). The present study demonstrates that the glymphatic pathway, a novel contributor to the macroscopic clearance of protein from the CNS interstitium, is sharply impaired by natural aging. The fact that such a macroscopic pathway for the re-circulation of CSF throughout the brain tissue may also contribute to the distribution of growth factors, neuromodulators, carrier proteins and other solutes also appears likely, while the failure of this distribution in the aging brain may have important pathophysiological consequences. These results suggest several largely unexplored mechanisms by which aging may contribute to declining cognitive function in aging and in neurodegenerative diseases, and on the basis of the present observations we propose that loss of perivascular AQP4 polarization and the reduction of cerebral arterial pulsatility may represent important therapeutic targets to restore paravascular CSF-ISF exchange in the aging brain.

Acknowledgments

The authors thank Dr. Charles Nicholson (New York University) for assistance in the analysis of TMA micro-iontophoresis recordings. This work was supported by funding from NIH/National institute of Neurological Disorders and Stroke (NS078167 and NS078304 to MN and NS073373 to JI) and the American Heart Association (12SDG11820014 to JI).

References

1. Lindsay J, Laurin D, Verreault R, Hebert R, Helliwell B, Hill GB, McDowell I. Risk factors for Alzheimer's disease: a prospective analysis from the Canadian Study of Health and Aging. Am J Epidemiol. 2002; 156:445–453. [PubMed: 12196314]
2. Ross CA, Poirier MA. Protein aggregation and neurodegenerative disease. Nat Med. 2004; 10(Suppl):S10–S17. [PubMed: 15272267]
3. Mawuenyega KG, Sigurdson W, Ovod V, Munsell L, Kasten T, Morris JC, Yarasheski KE, Bateman RJ. Decreased clearance of CNS beta-amyloid in Alzheimer's disease. Science. 2010; 330:1774. [PubMed: 21148344]
4. Iliff JJ, Wang M, Liao Y, Plogg BA, Peng W, Gundersen GA, Benveniste H, Vates GE, Deane R, Goldman SA, et al. A paravascular pathway facilitates CSF flow through the brain parenchyma and the clearance of interstitial solutes, including amyloid beta. Sci Transl Med. 2012; 4:147ra111.
5. Iliff JJ, Lee H, Yu M, Feng T, Logan J, Nedergaard M, Benveniste H. Brain-wide pathway for waste clearance captured by contrast-enhanced MRI. J Clin Invest. 2013; 123:1299–1309. [PubMed: 23434588]
6. Xie L, Kang H, Xu Q, Chen MJ, Liao Y, Thiyagarajan M, O'Donnell J, Christensen DJ, Nicholson C, Iliff JJ, et al. Sleep drives metabolite clearance from the adult brain. Science. 2013; 342:373–377. [PubMed: 24136970]
7. Iliff JJ, Wang M, Zeppenfeld DM, Venkataraman A, Plog BA, Liao Y, Deane R, Nedergaard M. Cerebral arterial pulsation drives paravascular CSF-interstitial fluid exchange in the murine brain. J Neurosci. 2013; 33:18190–18199. [PubMed: 24227727]

8. Yang L, Kress BT, Weber HJ, Thiyagarajan M, Wang B, Deane R, Benveniste H, Iliff JJ, Nedergaard M. Evaluating glymphatic pathway function utilizing clinically relevant intrathecal infusion of CSF tracer. J Transl Med. 2013; 11:107. [PubMed: 23635358]

9. Bell RD, Sagare AP, Friedman AE, Bedi GS, Holtzman DM, Deane R, Zlokovic BV. Transport pathways for clearance of human Alzheimer's amyloid beta-peptide and apolipoproteins E and J in the mouse central nervous system. J Cereb Blood Flow Metab. 2007; 27:909–918. [PubMed: 17077814]

10. Deane R, Wu Z, Sagare A, Davis J, Du Yan S, Hamm K, Xu F, Parisi M, LaRue B, Hu HW, et al. LRP/amyloid beta-peptide interaction mediates differential brain efflux of Abeta isoforms. Neuron. 2004; 43:333–344. [PubMed: 15294142]

11. Cirrito JR, May PC, O'Dell MA, Taylor JW, Parsadanian M, Cramer JW, Audia JE, Nissen JS, Bales KR, Paul SM, et al. In vivo assessment of brain interstitial fluid with microdialysis reveals plaque-associated changes in amyloid-beta metabolism and half-life. J Neurosci. 2003; 23:8844–8853. [PubMed: 14523085]

12. Nicholson C. Ion-selective microelectrodes and diffusion measurements as tools to explore the brain cell microenvironment. J Neurosci Methods. 1993; 48:199–213. [PubMed: 8412303]

13. Ren Z, Iliff JJ, Yang L, Yang J, Chen X, Chen MJ, Giese RN, Wang B, Shi X, Nedergaard M. 'Hit & Run' model of closed-skull traumatic brain injury (TBI) reveals complex patterns of post-traumatic AQP4 dysregulation. J Cereb Blood Flow Metab. 2013; 33:834–845. [PubMed: 23443171]

14. Wang M, Iliff JJ, Liao Y, Chen MJ, Shinseki MS, Venkataraman A, Cheung J, Wang W, Nedergaard M. Cognitive deficits and delayed neuronal loss in a mouse model of multiple microinfarcts. J Neurosci. 2012; 32:17948–17960. [PubMed: 23238711]

15. Shibata M, Yamada S, Kumar SR, Calero M, Bading J, Frangione B, Holtzman DM, Miller CA, Strickland DK, Ghiso J, et al. Clearance of Alzheimer's amyloid-ss(1–40) peptide from brain by LDL receptor-related protein-1 at the blood-brain barrier. J Clin Invest. 2000; 106:1489–1499. [PubMed: 11120756]

16. Iliff JJ, Nedergaard M. Is there a cerebral lymphatic system? Stroke. 2013; 44:S93–S95. [PubMed: 23709744]

17. Rennels ML, Gregory TF, Blaumanis OR, Fujimoto K, Grady PA. Evidence for a 'paravascular' fluid circulation in the mammalian central nervous system, provided by the rapid distribution of tracer protein throughout the brain from the subarachnoid space. Brain Res. 1985; 326:47–63. [PubMed: 3971148]

18. Sykova E, Nicholson C. Diffusion in brain extracellular space. Physiol Rev. 2008; 88:1277–1340. [PubMed: 18923183]

19. Nagelhus EA, Ottersen OP. Physiological roles of aquaporin-4 in brain. Physiol Rev. 2013; 93:1543–1562. [PubMed: 24137016]

20. Nielsen S, Nagelhus EA, Amiry-Moghaddam M, Bourque C, Agre P, Ottersen OP. Specialized membrane domains for water transport in glial cells: high-resolution immunogold cytochemistry of aquaporin-4 in rat brain. J Neurosci. 1997; 17:171–180. [PubMed: 8987746]

21. Verkman AS, Binder DK, Bloch O, Auguste K, Papadopoulos MC. Three distinct roles of aquaporin-4 in brain function revealed by knockout mice. Biochim Biophys Acta. 2006; 1758:1085–1093. [PubMed: 16564496]

22. Mathiisen TM, Lehre KP, Danbolt NC, Ottersen OP. The perivascular astroglial sheath provides a complete covering of the brain microvessels: an electron microscopic 3D reconstruction. Glia. 2010; 58:1094–1103. [PubMed: 20468051]

23. Brightman MW, Reese TS. Junctions between intimately apposed cell membranes in the vertebrate brain. J Cell Biol. 1969; 40:648–677. [PubMed: 5765759]

24. Amiry-Moghaddam M, Ottersen OP. The molecular basis of water transport in the brain. Nat Rev Neurosci. 2003; 4:991–1001. [PubMed: 14682361]

25. Redzic ZB, Preston JE, Duncan JA, Chodobski A, Szmydynger-Chodobska J. The choroid plexus-cerebrospinal fluid system: from development to aging. Curr Top Dev Biol. 2005; 71:1–52. [PubMed: 16344101]

26. Hadaczek P, Yamashita Y, Mirek H, Tamas L, Bohn MC, Noble C, Park JW, Bankiewicz K. The "perivascular pump" driven by arterial pulsation is a powerful mechanism for the distribution of therapeutic molecules within the brain. Mol Ther. 2006; 14:69–78. [PubMed: 16650807]
27. Wang P, Olbricht WL. Fluid mechanics in the perivascular space. J Theor Biol. 2011; 274:52–57. [PubMed: 21241713]
28. Schley D, Carare-Nnadi R, Please CP, Perry VH, Weller RO. Mechanisms to explain the reverse perivascular transport of solutes out of the brain. J Theor Biol. 2006; 238:962–974. [PubMed: 16112683]
29. Picano E, Bruno RM, Ferrari GF, Bonuccelli U. Cognitive impairment and cardiovascular disease: So near, so far. Int J Cardiol. 2014
30. Fonck E, Feigl GG, Fasel J, Sage D, Unser M, Rufenacht DA, Stergiopulos N. Effect of aging on elastin functionality in human cerebral arteries. Stroke. 2009; 40:2552–2556. [PubMed: 19478233]
31. Hughes TM, Kuller LH, Barinas-Mitchell EJ, Mackey RH, McDade EM, Klunk WE, Aizenstein HJ, Cohen AD, Snitz BE, Mathis CA, et al. Pulse wave velocity is associated with beta-amyloid deposition in the brains of very elderly adults. Neurology. 2013; 81:1711–1718. [PubMed: 24132374]
32. Zhang ET, Inman CB, Weller RO. Interrelationships of the pia mater and the perivascular (Virchow-Robin) spaces in the human cerebrum. J Anat. 1990; 170:111–123. [PubMed: 2254158]
33. Verkman AS, Mitra AK. Structure and function of aquaporin water channels. Am J Physiol Renal Physiol. 2000; 278:F13–F28. [PubMed: 10644652]
34. Salminen A, Ojala J, Kaarniranta K, Haapasalo A, Hiltunen M, Soininen H. Astrocytes in the aging brain express characteristics of senescence-associated secretory phenotype. Eur J Neurosci. 2011; 34:3–11. [PubMed: 21649759]
35. Hoshi A, Yamamoto T, Shimizu K, Ugawa Y, Nishizawa M, Takahashi H, Kakita A. Characteristics of aquaporin expression surrounding senile plaques and cerebral amyloid angiopathy in Alzheimer disease. J Neuropathol Exp Neurol. 2012; 71:750–759. [PubMed: 22805778]
36. Yang J, Lunde LK, Nuntagij P, Oguchi T, Camassa LM, Nilsson LN, Lannfelt L, Xu Y, Amiry-Moghaddam M, Ottersen OP, et al. Loss of astrocyte polarization in the tg-ArcSwe mouse model of Alzheimer's disease. J Alzheimers Dis. 2011; 27:711–722. [PubMed: 21891870]
37. May C, Kaye JA, Atack JR, Schapiro MB, Friedland RP, Rapoport SI. Cerebrospinal fluid production is reduced in healthy aging. Neurology. 1990; 40:500–503. [PubMed: 2314595]
38. Erickson MA, Hartvigson PE, Morofuji Y, Owen JB, Butterfield DA, Banks WA. Lipopolysaccharide impairs amyloid beta efflux from brain: altered vascular sequestration, cerebrospinal fluid reabsorption, peripheral clearance and transporter function at the blood-brain barrier. J Neuroinflammation. 2012; 9:150. [PubMed: 22747709]
39. Cserr HF. Physiology of the choroid plexus. Physiol Rev. 1971; 51:273–311. [PubMed: 4930496]
40. Groothuis DR, Vavra MW, Schlageter KE, Kang EW, Itskovich AC, Hertzler S, Allen CV, Lipton HL. Efflux of drugs and solutes from brain: the interactive roles of diffusional transcapillary transport, bulk flow and capillary transporters. J Cereb Blood Flow Metab. 2007; 27:43–56. [PubMed: 16639426]
41. Frost B, Diamond MI. Prion-like mechanisms in neurodegenerative diseases. Nat Rev Neurosci. 2010; 11:155–159. [PubMed: 20029438]

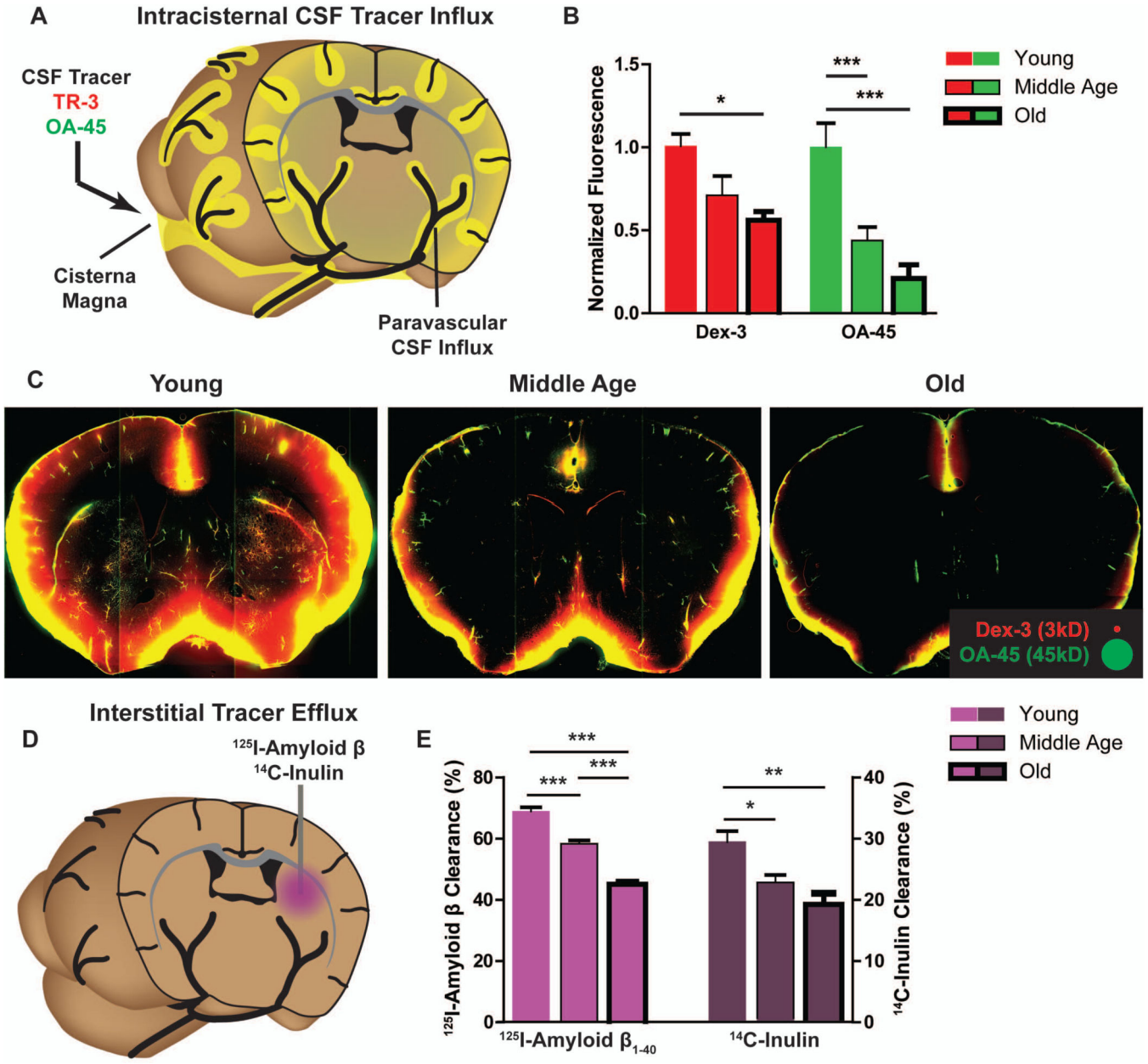

Figure 1. Age-dependent decline in paravascular glymphatic CSF recirculation and interstitial solute efflux

(A) Small molecular weight (Texas Red-conjugated dextran, 3 kD; Dex-3) and large molecular weight tracer (ovalbumin-conjugated ALEXA-647, 45 kD; OA-45) were injected intracisternally into young (2–3 months), middle age (10–12 months) and old (18 months) mice. **(B)** 30 min after injection, animals were perfusion fixed and whole-slice fluorescence was evaluated. CSF tracer penetration was significantly reduced in the old brain compared to the young brain, while values in the middle age brains were intermediate (*P<0.05, ***P<0.001; 1-way ANOVA; n = 5–8 per group). **(C)** Representative images show that compared to young brains, CSF tracer penetration into middle age and old brains is markedly slowed. **(D)** Radio-labeled ^{125}I-amyloid $\beta_{1–40}$ and ^{14}C-Inulin were co-injected into

the caudate nucleus of young, middle aged and old mice. 60 min after injection, solute clearance was evaluated by gamma counting and liquid scintillation counting. **(E)** Compared to clearance in the young brain, ^{125}I-amyloid $\beta_{1–40}$ and ^{14}C-Inulin clearance were significantly impaired in the old month brain (***P<0.001, **P<0.01, *P<0.05, 1-way ANOVA; n = 6–11 per group). ^{125}I-amyloid $\beta_{1–40}$ and ^{14}C-Inulin clearance in the middle age brain were intermediate between that of the young and old brain.

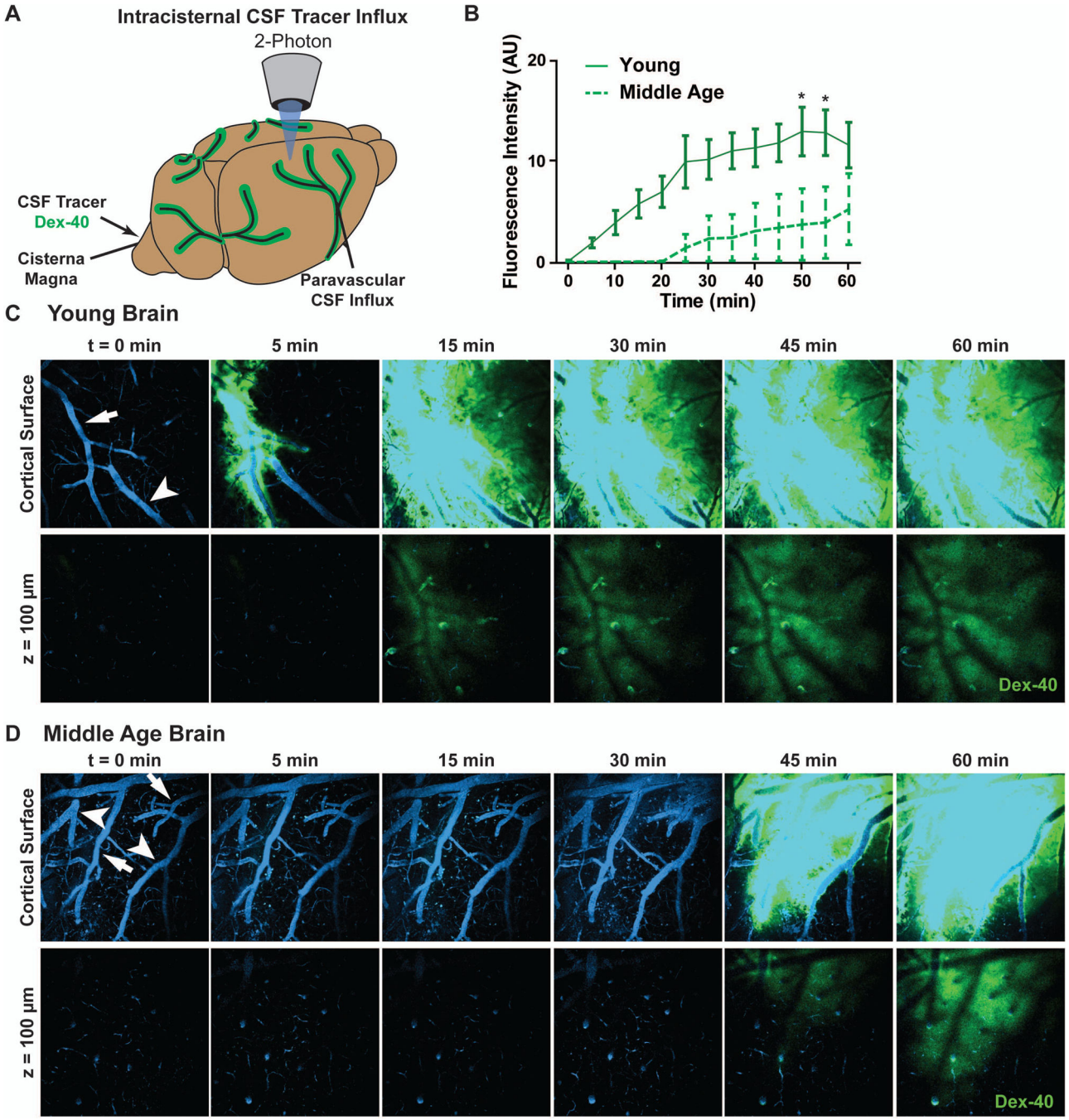

Figure 2. In vivo 2-photon imaging reveals suppressed paravascular glymphatic CSF recirculation in aging mice

(A) Paravascular CSF tracer penetration into the mouse cortex was evaluated by in vivo 2-photon microscopy after intracisternal injection of FITC-conjugated dextran (40 kD, Dex-40). **(B)** Quantification of CSF tracer penetration 100 µm below the cortical surface shows impaired paravascular penetration in middle age compared to young cortex (*P<0.05, 2-way repeated measures ANOVA; n = 4 animals per group). **(C-D)** Serial in vivo 2-photon imaging at the cortical surface and 100 µm below the cortical surface after intracisternal

Dex-40 injection. Cerebral vasculature is visualized by intra-arterial injection of Texas Red-conjugated dextran (70 kD, Dex-70, blue); surface arteries (arrows) and veins (arrowheads) are defined morphologically. Compared to the young brain **(C)**, CSF tracer movement along the surface and penetrating arteries and into the surrounding interstitium is markedly slowed in the middle age brain **(D)**.

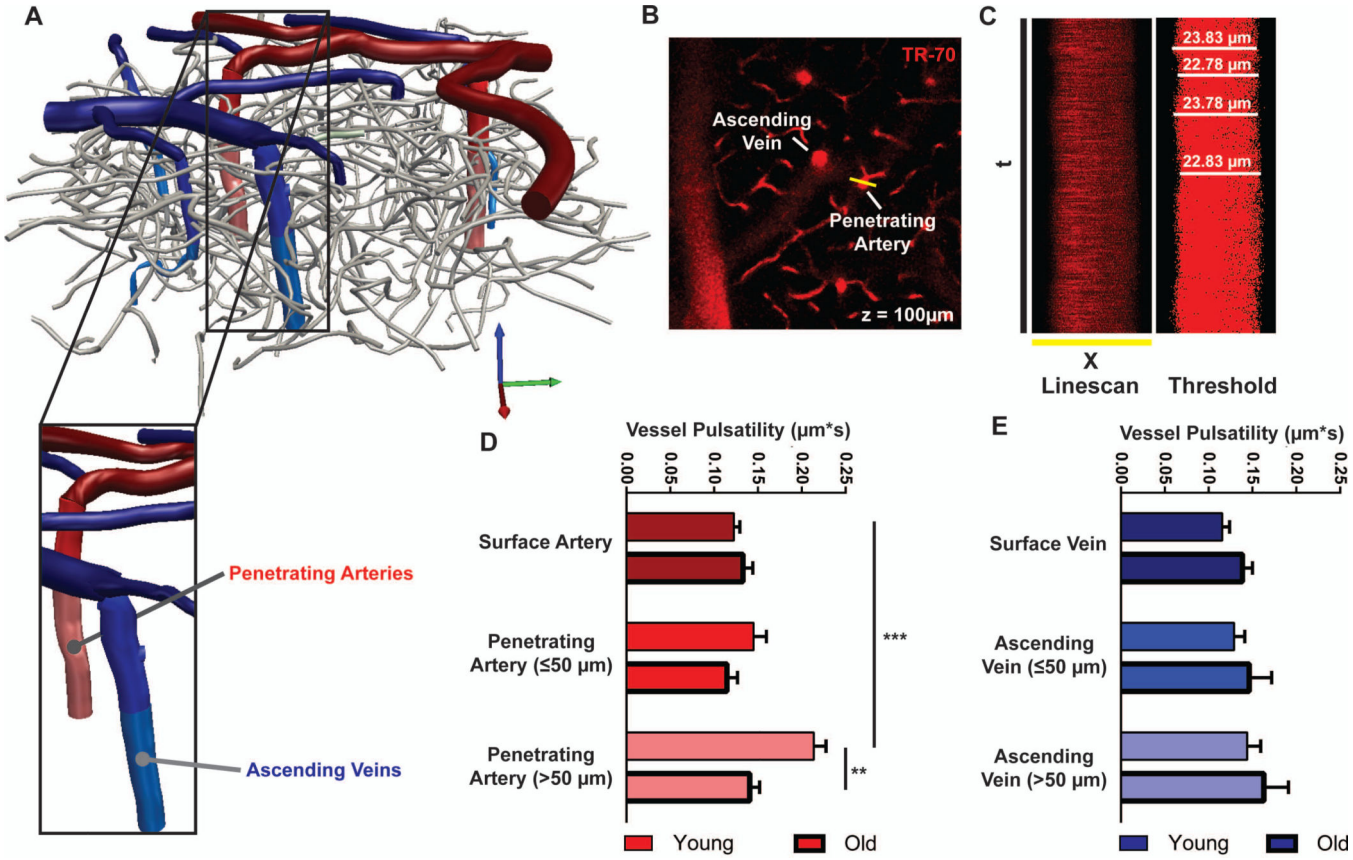

Figure 3. Vascular pulsatility is suppressed in the penetrating arteries of the aging brain

Pulsatility of the vascular wall was evaluated by in vivo 2-photon microscopy through thin-skull cranial window after intra-arterial injection of Texas Red-conjugated dextran (MW 70kD, dex-70). **(A)** 3D reconstruction of the cerebrovascular tree visible through cranial window reveals penetrating arteries (red), ascending veins (blue) and intervening capillary bed (gray). **(B)** Between z = 0 and 150 µm below the cortical surface, high-frequency orthogonal linescans were generated across surface and penetrating arteries and surface and ascending veins. **(C)** Representative raw x-t scans were thresholded to improve edge detection, and the luminal diameter was measured over time. **(D-E)** Vascular pulsatility was measured from penetrating arteries and ascending veins. In the young brain, arterial pulsatility was significantly greater than venous pulsatility (*P<0.05, 2-way ANOVA; n = 8–20 vessels from 4 animals per group). In the old brain, arterial pulsatility in the penetrating arteries was significantly reduced compared to the young brain (*P<0.05, Young vs. Old). No age-related differences in venous pulsatility were observed.

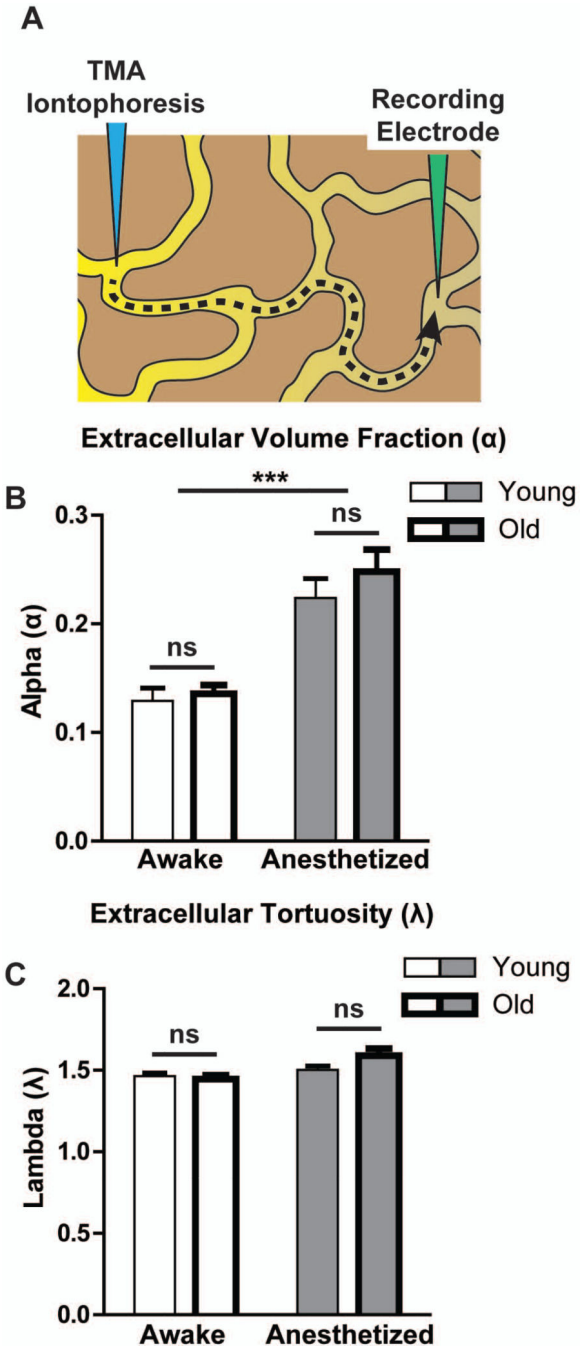

Figure 4. Interstitial volume does not change as a function of aging

(A) Extracellular volume fraction (α) and tortuosity (λ) were evaluated by the in vivo TMA micro-iontophoresis method. TMA is introduced by an iontophoresis electrode and detected by a second recording electrode. Changes in the extracellular volume fraction or the tortuosity of the extracellular space are reflected in the kinetics of the measured TMA concentrations (described in detail in(18)). **(B)** In the cortex of either awake or anesthetized mice, extracellular volume fraction did not significantly differ between young and old animals. Both young and old brains exhibited a significant and comparable enlargement of

the extracellular space in the anesthetized state (***P<0.001, Awake vs. Anesthetized; 2-Way ANOVA; n = 9–20 per group). **(C)** Extracellular tortuosity did not differ significantly between young and old animals.

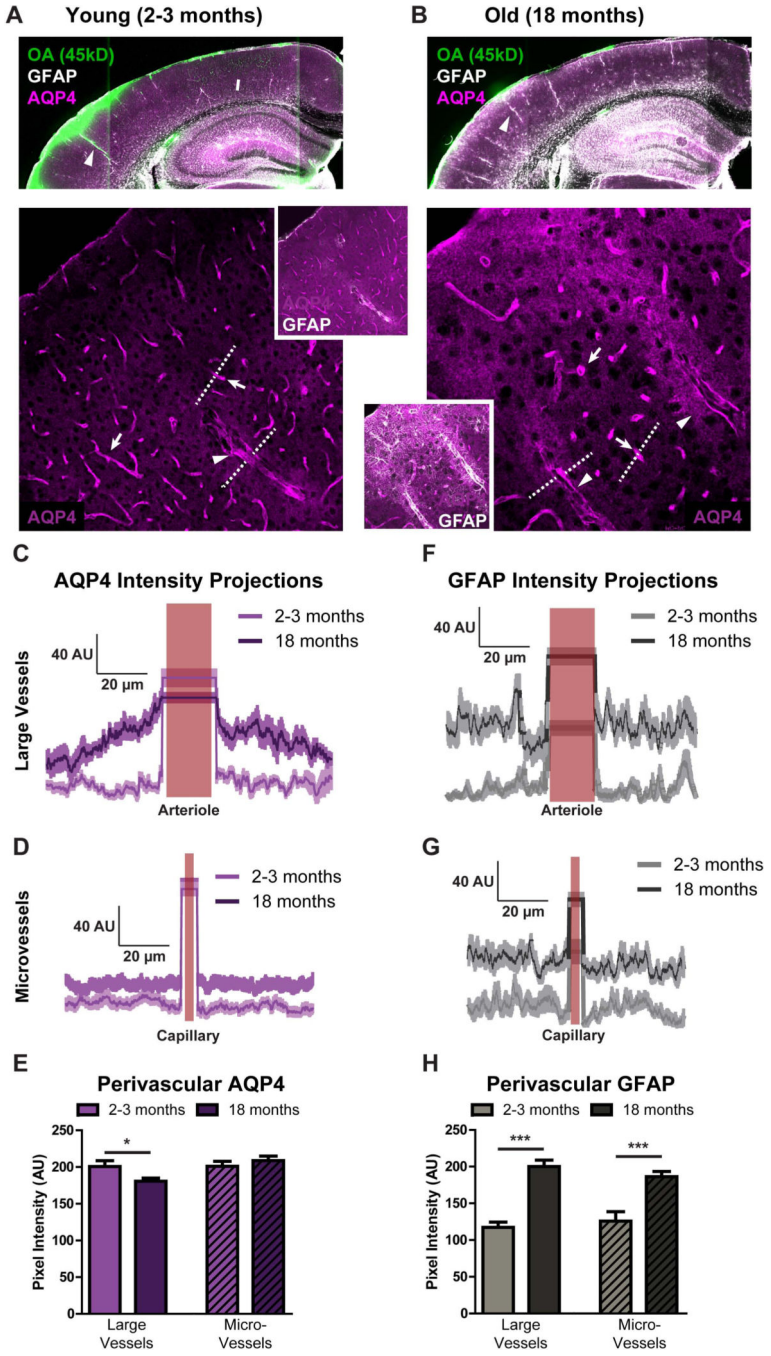

Figure 5. Perivascular AQP4 polarization surrounding penetrating arteries is lost in the aging brain

Changes in AQP4 localization, GFAP expression and paravascular CSF recirculation were evaluated by immunofluorescence double-labeling. **(A-B)** Slices from brains fixed 30 min after intracisternal injection of fluorescent CSF tracer ovalbumin-conjugated ALEXA-647 (MW 45kD, OA-45) were imaged by confocal microscopy and show that compared to the young cortex **(A)**, AQP4 localization becomes more disperse in the old brain while GFAP expression increases and CSF tracer penetration is slowed **(B)**. AQP4 and GFAP

immunofluorescence were evaluated in linear regions of interest (dashed lines) extending outward from penetrating cerebral arterioles (arrowheads, **C, F**) or outward from cerebral capillaries (arrows, **D, G**). **(C-D, F-G)** Compared to the young brain, and GFAP expression were increased surrounding blood vessels in the aging brain (***P<0.001, young vs. old; repeated measures 2-way ANOVA; n = 11–18 vessels from 4 animals per group). Changes in AQP4 expression were greater surrounding penetrating arterioles **(C)** than cortical capillaries **(B)**, with marked upregulation of AQP4 in tissue surrounding penetrating vessels. Measurement of perivascular AQP4 **(E)** and GFAP **(H)** expression showed that AQP4 is downregulated in perivascular domains surrounding penetrating arterioles, but not around capillaries (*P< 0.05; un-paired t-test, n = 11–18 vessels from 4 animals per group) while perivascular GFAP expression was similarly upregulated surrounding both vessel types (***P<0.001; un-paired t-test).

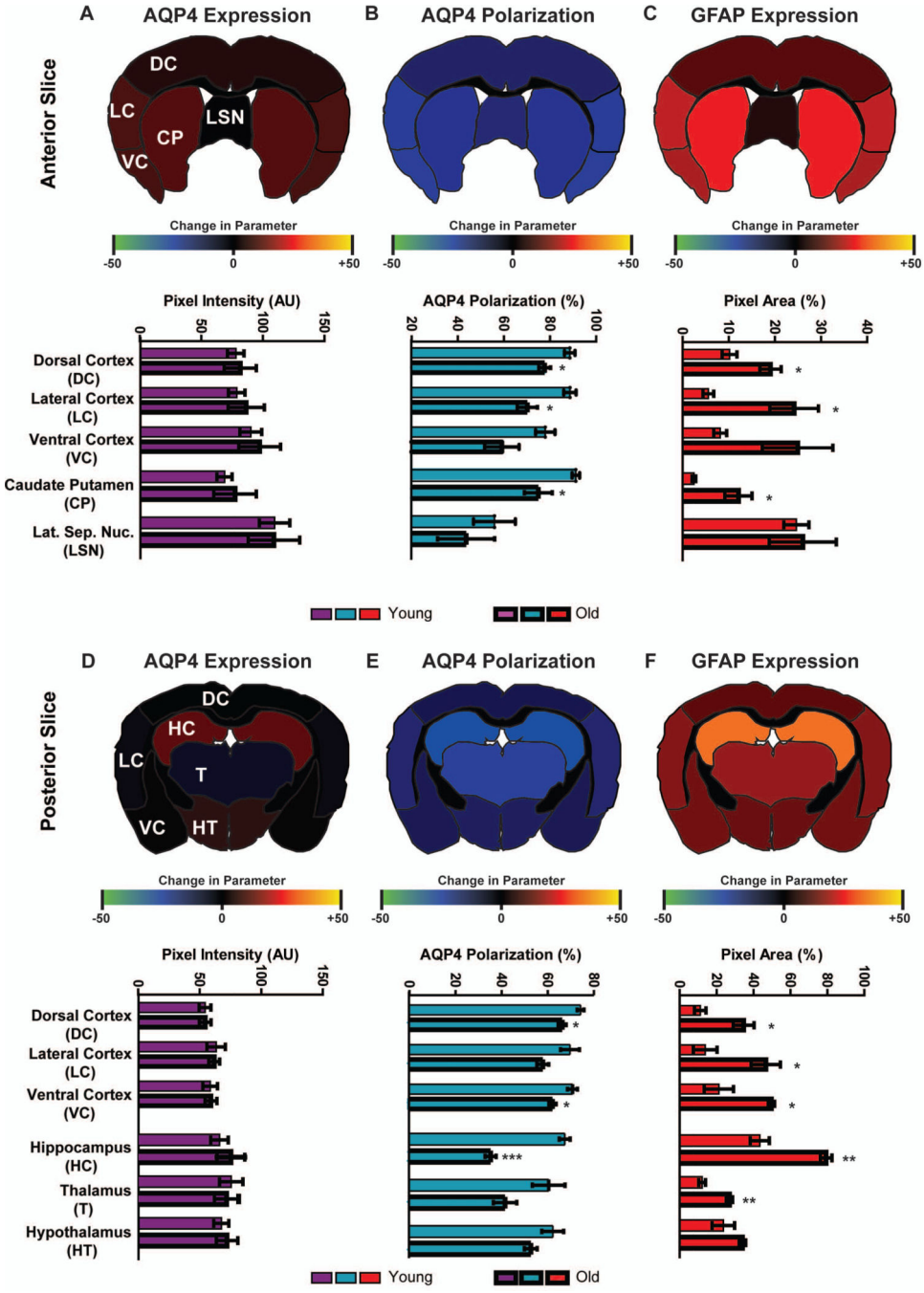

Figure 6. Impairment of perivascular AQP4 polarization is greatest in the lateral and ventral cortex, hippocampus and striatum of the aging brain

AQP4 expression and polarization and GFAP expression were evaluated by immunofluorescence in fixed brain slices from young (2–3 month) and old (18 month) brains. Expression and polarization were evaluated within different regions of anterior **(A-C)** and posterior **(D-F)** brain slices. Regional heat maps depict mean change in AQP4 expression (AQP4 immunofluorescence), AQP4 polarization (% area), and GFAP expression (% area) between young and old brains. (**A, D**) Within both the anterior and

posterior regions, global AQP4 immunofluorescence did not differ between the young and old brains. **(B, E)** Perivascular AQP4 polarization was significantly reduced in the aged brain, with most pronounced effects in the lateral and ventral cortex, striatum and hippocampus (*P<0.05, **P<0.01, ***<0.001, Young vs. Old; 2-way ANOVA; n = 4 per group). **(C, F)** GFAP expression was significantly increased in the old compared to the young brain, with the greatest effect evident within the lateral and ventral cortex, hippocampus and striatum (*P<0.05, **P<0.01, ***<0.001, Young vs. Old; 2-way ANOVA; n = 4 per group).

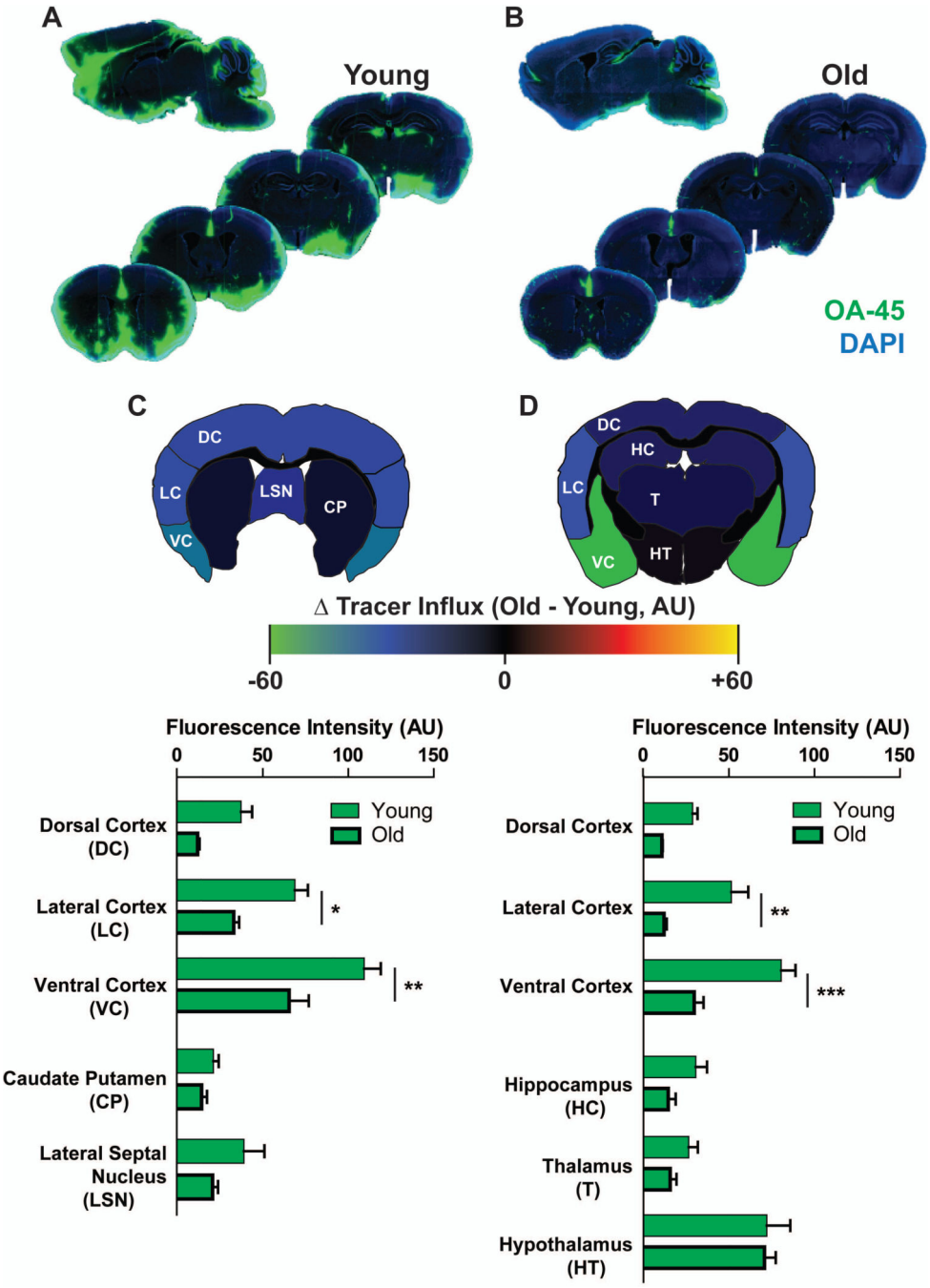

Figure 7. Ventral and lateral cortex exhibit the most severe suppression of glymphatic pathway activity in the aged brain

Age-related impairment of paravascular CSF recirculation was evaluated 30min after intracisternal injection of small molecular weight CSF tracer Texas Red-conjugated dextran (MW 3kD, Dex-3) and large molecular weight ovalbumin-conjugated ALEXA 647 (MW 45kD, OA-45). Representative saggital and coronal slices from young **(A)** and old **(B)** brains show marked reduction in CSF tracer penetration throughout the aged compared to the young brain. CSF tracer penetration within defined brain regions was evaluated and heat

maps from anterior **(C)** and posterior **(D)** slices depict the change in mean OA-45 CSF tracer penetration observed in each region between old and young brains. Quantification of OA-45 penetration in different regions showed that paravascular CSF recirculation was significantly impaired in the lateral and ventral cortex of both the anterior and posterior slices (*P<0.05, **P<0.01, ***P<0.001, Young vs. Old; 2-way ANOVA; n = 4 per group).

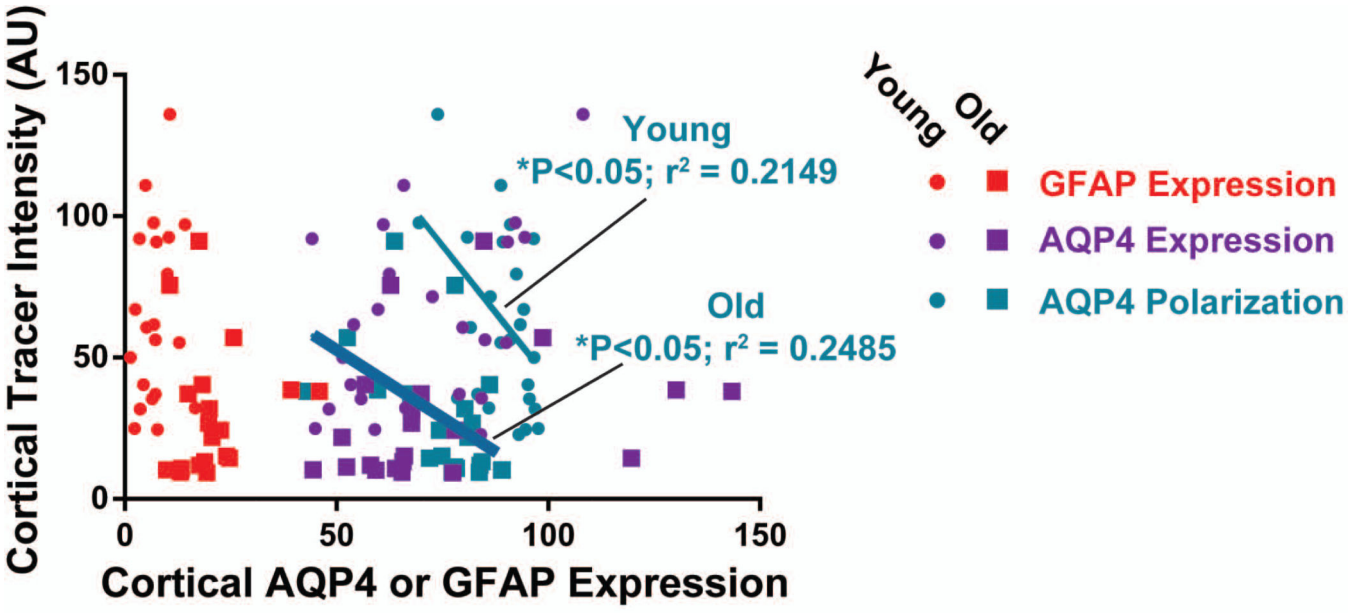

Figure 8. Loss of cortical perivascular AQP4 polarization is associated with impaired paravascular CSF recirculation

(A) The association between AQP4 expression, AQP4 polarization or GFAP expression and paravascular CSF tracer was evaluated in the cortex. Linear regression analysis shows that GFAP and AQP4 expression levels were not associated with differences in paravascular CSF tracer penetration in the young or old cortex. Within both the young and old cortex, reduction in perivascular AQP4 polarization were significantly associated with impairment of paravascular CSF recirculation (Young brain: *P<0.05, r^2 = 0.2149; Old brain: *P<0.05, r^2 = 0.2485).

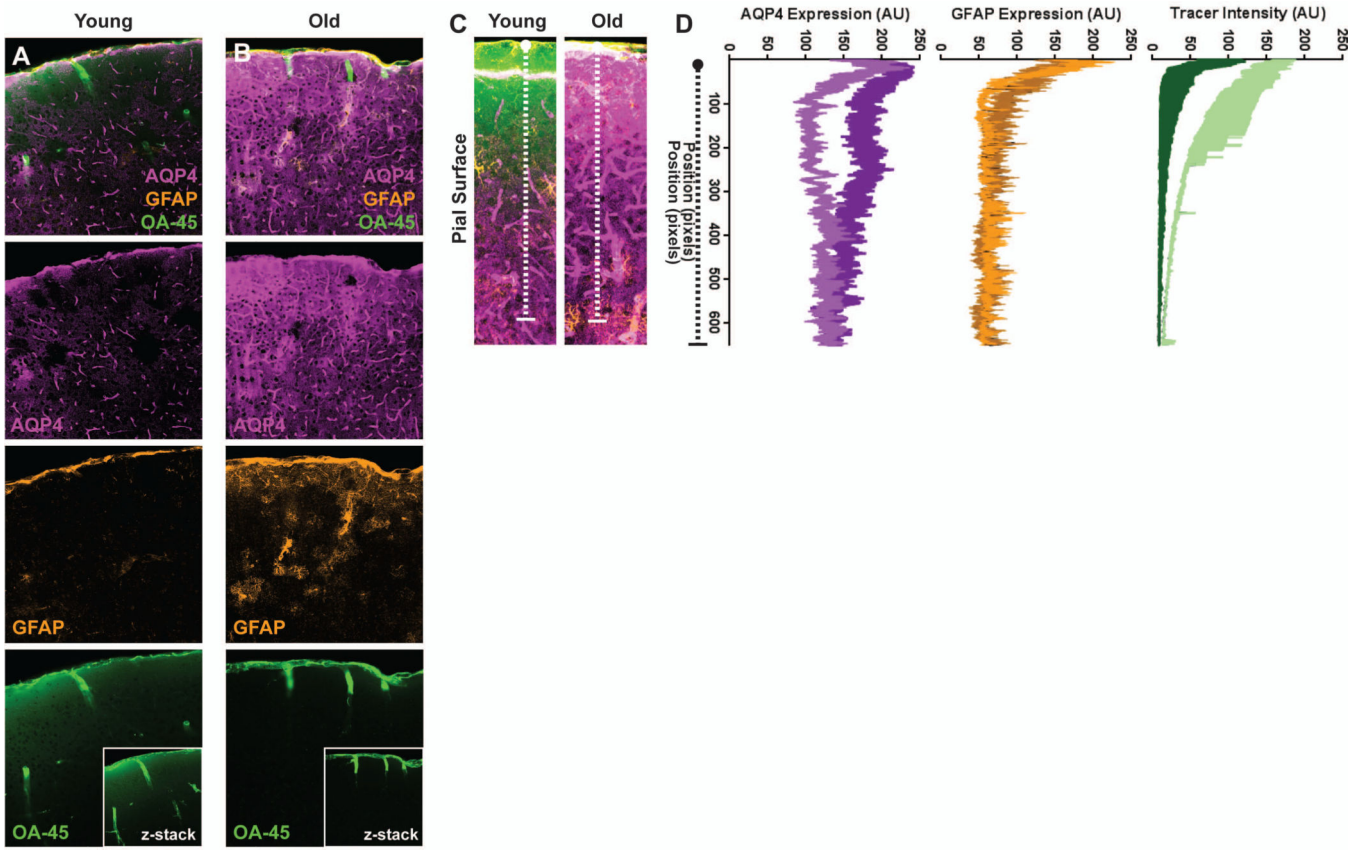

Figure 9. Increased pial surface AQP4 expression is associated with impaired trans-pial CSF penetration

The association between changes in subpial AQP4 and GFAP expression and trans-pial CSF tracer penetration were evaluated in the lateral cerebral cortex of young **(A)** and old **(B)** mice. **(C)** AQP4 and GFAP expression and CSF tracer intensity were evaluated in linear regions of interest (white dashed lines) extending inward from the pial surface. **(D)** Compared to the young brain, AQP4 expression in the aging brain was significantly greater near the pial surface (**P<0.01, Young vs. Old; 2-way repeated measures ANOVA, n = 6–8 per group) while GFAP immunoreactivity was not significantly altered. Increased sub-pial AQP4 expression in the aging brain was associated with a significant reduction in trans-pial CSF tracer penetration (**P<0.01, Young vs. Old; 2-way repeated measures ANOVA, n = 6–8 per group).